

Electron beam powder bed fusion of Ti-30Ta high-temperature shape memory alloy: microstructure and phase transformation behaviour

C. Lauhoff, M. Nobach, A. Medvedev, T. Arold, C. Torrent, J. Elambasseril, P. Krooß, M. Stenzel, M. Weinmann, W. Xu, A. Molotnikov & T. Niendorf

To cite this article: C. Lauhoff, M. Nobach, A. Medvedev, T. Arold, C. Torrent, J. Elambasseril, P. Krooß, M. Stenzel, M. Weinmann, W. Xu, A. Molotnikov & T. Niendorf (2024) Electron beam powder bed fusion of Ti-30Ta high-temperature shape memory alloy: microstructure and phase transformation behaviour, *Virtual and Physical Prototyping*, 19:1, e2358107, DOI: [10.1080/17452759.2024.2358107](https://doi.org/10.1080/17452759.2024.2358107)

To link to this article: <https://doi.org/10.1080/17452759.2024.2358107>



© 2024 The Author(s). Published by Informa UK Limited, trading as Taylor & Francis Group



[View supplementary material](#)



Published online: 19 Jun 2024.



[Submit your article to this journal](#)


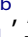

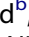
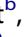









[View related articles](#)



[View Crossmark data](#)

Electron beam powder bed fusion of Ti-30Ta high-temperature shape memory alloy: microstructure and phase transformation behaviour

C. Lauhoff ^{a,b}, M. Nobach ^b, A. Medvedev ^a, T. Arold ^b, C. Torrent ^b, J. Elambasseril ^a, P. Krooß ^b, M. Stenzel ^c, M. Weinmann ^c, W. Xu ^{a,d}, A. Molotnikov ^a and T. Niendorf ^b

^aRMIT Centre for Additive Manufacturing, Carlton, Australia; ^bInstitute of Materials Engineering, University of Kassel, Kassel, Germany; ^cTANIOBIS GmbH, Goslar, Germany; ^dSchool of Engineering, Deakin University, Geelong, Australia

ABSTRACT

The present study reports on additive manufacturing of a Ti-30Ta (at.%) high-temperature shape memory alloy (HT-SMA) using electron beam powder bed fusion (PBF-EB/M) technique. Detailed microstructure analysis was conducted to reveal the microstructural evolution along the entire process chain, i.e. from gas-atomised powder to post-processed material. PBF-EB/M processed structures with near full density and an isotropic, β -phase stabilised microstructure, i.e. equiaxed β -grains of around 20 μm in diameter with no preferred crystallographic orientation, are reported. As revealed by differential scanning calorimetry, post-process heat-treated Ti-Ta demonstrates a reversible martensitic phase transformation well above 100°C. Although partly unmolten Ta-particles after both gas atomisation and PBF-EB/M remain a challenge towards robust processing, PBF-EB/M appears to show significant potential for fabrication of Ti-Ta HT-SMAs, especially when functional metal parts and components with complex shapes are required, which are difficult to fabricate conventionally.

ARTICLE HISTORY

Received 24 February 2024

Accepted 13 May 2024

KEYWORDS

Additive manufacturing; pre-alloyed powder; ELGA; refractory metals; martensitic phase transformation



1. Introduction


1.1. Shape memory alloys

Shape memory alloys (SMAs) represent a class of smart materials and have received significant scientific attention over the past decades. Their unique functional properties, i.e. shape memory effect (SME) and superelasticity (SE), are based on a reversible solid-state phase transformation between a high-temperature parent austenitic phase and a low-temperature product martensitic phase [1,2]. Due to large reversible transformation strains, SMAs are very attractive for designing compact and efficient solid-state actuators and damping devices [1,3]. To date, binary Ni-Ti alloys are the most widely employed SMAs. As it is highly biocompatible, this system is currently the material of choice for biomedical applications, such as orthodontic wires and stents. However, the inherent application temperature limit of about 80°C hinders its technological breakthrough in fields like the aerospace and energy sectors or the chemical industry, where operating temperatures often exceed 100°C [1–5].

1.2. The Ti-Ta high-temperature shape memory alloy system

Alloy systems with phase transformation temperatures above 100°C, referred to as high-temperature (HT-) SMAs, have been introduced in recent years [6]. Today, most of the HT-SMA systems with promising shape memory characteristics comprise ternary Ni-Ti based alloys [6–8]. Unfortunately, these alloys rely on high contents of highly expensive noble metals like Pd and Pt (e.g. 30 wt.%) or are inherently brittle [6]. In this regard, Ti-Ta alloys represent a promising alternative to overcome these issues: this alloy system features good ductility and workability [9,10] and only contains reasonably prized constituents, even though it should be noted that Ta is not a low-cost metal. Furthermore, these β -Ti based alloys show shape memory properties at elevated temperatures. Their functional performance is based on a martensitic transformation between the austenitic β -phase with body-centered cubic (bcc) lattice structure and the martensitic α'' -phase (orthorhombic). Exploitable transformation strains of up to 3.6% can be obtained [11]. The transformation temperatures, in turn, show a strong

CONTACT C. Lauhoff  lauhoff@uni-kassel.de  RMIT Centre for Additive Manufacturing, 58 Cardigan St., Carlton, VIC 3083, Australia; Institute of Materials Engineering, University of Kassel, Mönchebergstr. 3, Kassel 34125, Germany

 Supplemental data for this article can be accessed online at <https://doi.org/10.1080/17452759.2024.2358107>

© 2024 The Author(s). Published by Informa UK Limited, trading as Taylor & Francis Group

This is an Open Access article distributed under the terms of the Creative Commons Attribution License (<http://creativecommons.org/licenses/by/4.0/>), which permits unrestricted use, distribution, and reproduction in any medium, provided the original work is properly cited. The terms on which this article has been published allow the posting of the Accepted Manuscript in a repository by the author(s) or with their consent.

dependence on the chemical composition, i.e. they increase by roughly 25–30 K/at.% with decreasing Ta concentration [12,13], and can exceed 400°C when the Ta content is reduced to 20 at.% [14].

Unfortunately, binary Ti-Ta HT-SMAs do not comply with all demands of robust industrial application. Previous studies indicate that this alloy system suffers a lack of functional/microstructural stability under thermal and thermo-mechanical cycling [9,11,13,15–17]. This behaviour is primarily linked to the precipitation of the hexagonal ω -phase, which is also found in similar alloys like Ti-Nb [18,19]. The formation of the Ti-rich ω -phase leads to the stabilisation of the austenitic β -phase, consequently causing a loss of the functional properties. The kinetics of the ω -phase evolution and, thus, the rate of functional degradation have been reported to be strongly dependent on the time-temperature profile during thermo-mechanical loading, i.e. applied heating/cooling rates and maximum test temperatures [15,16]. Interestingly, the addition of ternary alloying elements such as Al and Sc can suppress ω -phase formation [13,20–25]. Likewise, short-time recovery heat treatments to dissolve precipitated ω -phase particles were shown to be a promising approach to qualify Ti-Ta based alloys for stable high-temperature actuation responses [11,15].

1.3. Additive manufacturing of (high-temperature) shape memory alloys

Nowadays, metal additive manufacturing (AM) technologies, especially powder bed fusion (PBF) processes and directed energy deposition (DED), are widely adopted in academia and industry. In contrast to traditional metallurgical processing routes, functional metal parts and components of unprecedented geometrical complexity can be fabricated by melting successive layers of a metallic feedstock material [26,27]. In recent years, a variety of alloys and classes of materials were qualified for these technologies to open up new industrial markets [28,29]. In case of SMAs, the possibility for a tool-free design allows for realisation of new and innovative actuator designs by AM technologies. Consequently, extensive research activities in the field of AM of SMAs are currently ongoing and substantial progress has been already made. The majority of work focused on Ni-Ti [30,31], but also ternary Ni-Ti alloys such as Ni-Ti-Hf [32,33], Cu-based [34,35], Ni-Mn-based [36,37], and Co-Ni-Ga [38,39] were examined. In contrast, work on additively manufactured Ti-Ta HT-SMAs bulk structures is still completely missing. Only the synthesis of Ti-Ta shape memory surface coatings by an electron beam based additive technology has been reported recently [40]. In order to tackle this prevailing

gap in literature, pre-alloyed Ti-Ta HT-SMA powder was processed for the first time by electron beam powder bed fusion (PBF-EB/M). In comparison to laser beam powder bed fusion (PBF-LB/M), the PBF-EB/M technique is usually characterised by higher processing temperatures and takes place under controlled vacuum atmosphere [26,27]. In consequence, both the residual stresses and impurity concentration caused by oxygen pickup are lower compared to PBF-LB/M processing. Especially due to the latter, PBF-EB/M recently emerged considerable attention for processing of metals and alloys, suffering from high oxygen affinity [41–43]. Beside the general processability, in the present study, the microstructure and martensitic phase transformation behaviour have been thoroughly investigated. Hereto, the powder feedstock material as well as PBF-EB/M processed structures in both as-built and post-process heat-treated condition were considered, enabling deep insights into an additively manufactured Ti-Ta HT-SMA along the entire process chain.

2. Material and methods

2.1. Material and processing

Pre-alloyed powder feedstock material with a nominal chemical composition of Ti-30Ta (at.%) was produced by electrode induction melting gas atomisation (EIGA) from pre-alloyed electrodes using purified argon gas (4.6, Linde). In the current work, this specific composition is considered, since in a series of previous studies the structural and functional properties of this alloy were already investigated [11,15,17,20], allowing for direct comparison between additively manufactured and conventionally processed material at this point. The chemical composition of the atomised powder is given in Table 1 and was investigated by inductively coupled plasma optical emission spectroscopy (ICP-OES; Analytik Jena PlasmaQuant PQ 9000/9100), carrier gas hot extraction (LECO TCH-600/ONH-836) and/or combustion analysis (LECO CS-744).

As the as-atomised powder featured minor fractions of coarse and/or irregular-shaped particles, the powder material was sieved using 150 μm meshes. Subsequently, the powder was transferred into an air classifier for deagglomeration and removal of fine particles <10 μm to improve flowability and avoid dusting during processing. From the remaining powder, the

Table 1. Chemical composition of the Ti-30Ta (at.%) powder material after EIGA process.

	Ti (at.%)	Ta (at.%)	C (ppm)	H (ppm)	N (ppm)	O (ppm)
Nominal	70	30	–	–	–	–
Measured	69.9	30.1	19	13	56	1048

PBF-EB/M particle size fraction (63–105 μm) was extracted by ultrasonic sieving with 63 and 105 μm stainless steel meshes, respectively. Particle size distributions (PSDs) were determined using a Mastersizer 2000 (Malvern, Worcestershire, United Kingdom). D_{10} , D_{50} , and D_{90} values are found to be 58.5, 79.44, and 107.66 μm , respectively.

A General Electric (GE) Additive Arcam A2X machine was used for PBF-EB/M processing. In order to limit the volume of required powder material, a build plate reduction was utilised. Cuboidal blocks with dimensions of $10 \times 10 \times 10 \text{ mm}^3$ were fabricated on a commercially pure titanium (CP-Ti) build plate with 40 mm in diameter. A bidirectional meander scanning strategy with 90° rotation between successive layers was applied. In each build, only a single cuboid was fabricated employing beam currents and beam speeds in a range of 10–15 mA and 2500–2700 mm/s, respectively. For the sake of brevity, only the material processed using the set of parameters leading to the highest density is detailed in the present study. An overview of these processing parameters is shown in Table 2. The values for the acceleration voltage, beam current, beam speed, and hatch distance lead to a resulting volumetric energy density of 66.67 J/mm^3 . Figure 1 depicts the corresponding temperature-time profile during processing and subsequent cooling that was measured within the build chamber using a thermocouple placed below the build plate. The time-temperature-transformation (TTT) diagram for the alloy composition investigated, i.e. Ti-30Ta (at.%), is included.

2.2. Sample preparation and characterisation

The PBF-EB/M manufactured cuboids were cut along the build direction (BD) and parallel to the lateral surfaces of

Table 2. Processing parameters used for PBF-EB/M of the Ti-Ta samples detailed in the present study.

Heating before process start	
Start temperature	540°C
Preheating	
Beam speed	12000 mm/s
Beam current ^a	5–10 mA
Focus offset	75 mA
Number of repetitions ^b	8 + 2
Melting	
Acceleration voltage	60 kV
Beam speed	2700 mm/s
Beam current	15 mA
Focus offset	3 mA
Hatch distance	0.1 mm
Layer thickness	0.05 mm

^aThe beam current was ramped up from 5 to 10 mA.

^bA total of 10 electron beam passes was conducted during preheating. While the beam current ramping was applied during the first 8 passes, the beam current was kept constant at its maximum value for the last two passes.

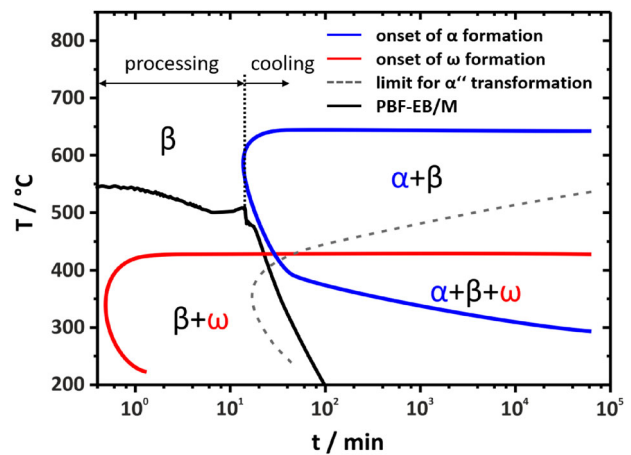


Figure 1. Temperature-time profile for PBF-EB/M processing of the Ti-Ta alloy and subsequent cooling. The TTT diagram for Ti-30Ta (at.%) adapted from [17] is superimposed.

the cuboids into plates of 1.5 mm thickness by electrodischarge machining (EDM). These plates were mechanically ground down to 15 μm grit size to remove the EDM-affected surface layer. The additively manufactured Ti-Ta was studied in two different material states, i.e. as-built and solution-annealed (25 h/1100°C). Solution-annealing was carried out in sealed quartz glass tubes under argon atmosphere to limit oxidation, followed by water quenching. Heat treatment parameters were chosen in accordance to Refs. [10,17]. Since the argon pressure within the quartz tubes was limited to values below 1 atm during the whole heat treatment procedure, the post-process heat treatment had no effect on the defect population and the relative density of the additively manufactured structures.

For scanning electron microscopy (SEM) analysis, the plates were embedded using a cold mounting epoxy resin and then ground down to 10 μm (P2000 grit paper) and additionally polished for 10 min using a 0.25 μm oxide polishing suspension (OP-S, Struers). Analysis of local chemical segregations and crystallographic texture was carried out using a JEOL 7200F system including units for backscatter electron (BSE) contrast (5 kV acceleration voltage, 3 nA current), energy-dispersive X-ray spectroscopy (EDS) (15 kV acceleration voltage, 3 nA current) and electron backscatter diffraction (EBSD) (20 kV acceleration voltage, 20 nA current). The plates investigated were extracted from the centre of the PBF-EB/M processed cuboids. Thus, micrographs presented in the following illustrate characteristic and representative findings. In addition to SEM, transmission electron microscopy (TEM) was employed to characterise the ω -phase. The TEM foils were prepared using a focused ion beam (FIB) milling and lift-out technique, performed with a FEI Scios Dual-beam FEGSEM at a nominal acceleration voltage of

30 kV. Selected area electron diffraction (SAED) was conducted using a JEOL 2100F FEGTEM at an acceleration voltage of 200 kV. Surface plots were created using the ImageJ 3D interactive plot plugin.

A GE Phoenix v-tome-xs 240 computed tomography (CT) system with a copper filter of 0.1 mm thickness was employed to capture process-induced defects. The CT was operated at 110 kV and 50 W. Images were recorded for 1 s per image during a 360° rotation using a step size of 0.15°. The system utilises a cone-shaped X-ray beam for magnification control. CT scanning was conducted at 6.5 µm voxel resolution with an average of three frames and two skips. The 3D volume reconstruction necessitated multiple projections of raw images that were facilitated by the Datos 2.2 software. Furthermore, the porosity analysis was conducted using VG Studio 3.0.

For phase composition analysis, X-ray diffraction (XRD) measurements were performed using a Panalytical Empyrian diffractometer equipped with a copper tube, a secondary monochromator providing Cu-Kα1 radiation, and a PIXcel3D detector. Diffraction intensities were recorded in a 2θ-range of 30–100° applying a step size of 0.01° and a measuring time of 5 s per step. Differential scanning calorimetry (DSC) was employed to evaluate the martensitic phase transformation behaviour. Specimens with masses of about 50 mg were investigated using a Perkin Elmer DSC Pyris 1. The heating/cooling rates were set to 20 K/min. Specimens were heated from 75°C to the maximum test temperature ($T_{\max} = 225^{\circ}\text{C}$), held for 3 min followed by subsequent cooling.

3. Results and discussion

3.1. Powder characterisation

Figure 2 shows secondary electron (SE) micrographs of the pre-alloyed Ti-Ta powder in the as-atomised and sieved

condition used for PBF-EB/M processing in the present work. As can be seen from Figure 2(a), a fully deagglomerated powder material has been obtained after the EIGA process and subsequent sieving. The particles are highly spherical and feature smooth surfaces free of defects like cracks. Only a few satellites on the particle surfaces (white arrows in Figure 2(b)) can be seen. These satellite particles are known to be formed by collisions in solid state and/or due to adhesion in liquid state [44].

Cross-section BSE images of polished powder particles recorded at different magnifications and an EDS mapping are shown in Figure 3. The particles exhibit a dendrite-type microstructure, where the inter-dendritic areas are enriched in Ti (Figure 3(c)). These chemical inhomogeneities, i.e. the formation of dendrite-type features, are attributed to the inherent cooling rates during powder synthesis by EIGA and, thus, are slightly influenced by the powder particle size considered. The microstructure seen is in agreement with previous results obtained for gas-atomised Al-modified Ti-Ta [45], Ti-42Nb [46], Ti-Nb-Ta [47] as well as powder metallurgically processed tungsten containing Ti-Al [48] powders. Occasionally, unmelted Ta-particles with diameters of up to 20 µm are also visible, which remained after the EIGA process (Figure 3(a)). It has to be noted that these Ta-particles were not fully dissolved during gas atomisation from pre-alloyed electrodes (s. chapter 2), and are not enrichments by element segregations. Thus, the Ta-particles will be termed as ‘unmelted’ in the remainder of the text.

3.2. Microstructure of PBF-EB/M processed Ti-Ta

3.2.1. As-built condition

Following processing of the pre-alloyed Ti-Ta powder feedstock material by PBF-EB/M, CT analysis was conducted for defect characterisation. Figure 4 shows a transparent colour-coded illustration of the defects

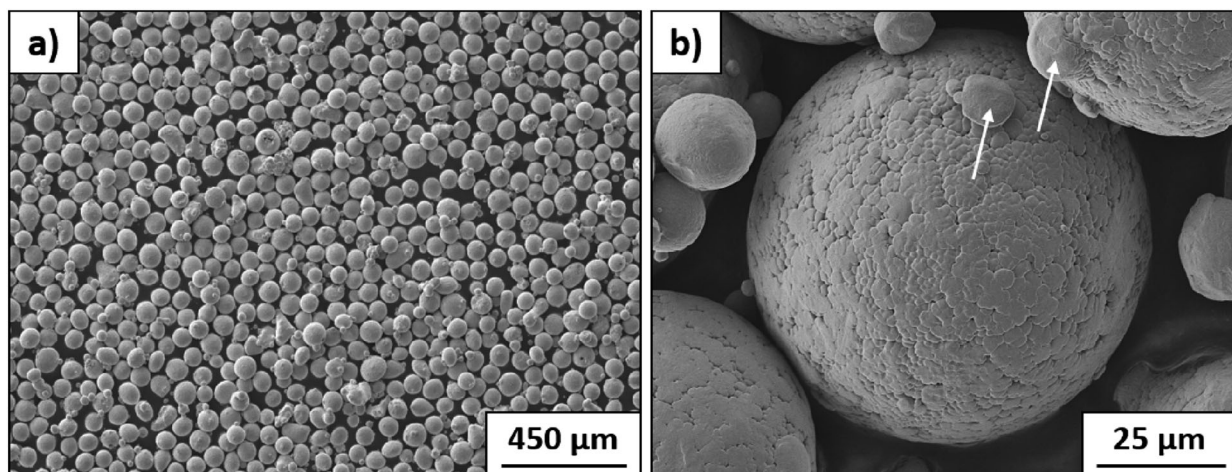


Figure 2. SE images of the pre-alloyed Ti-Ta powder feedstock material.

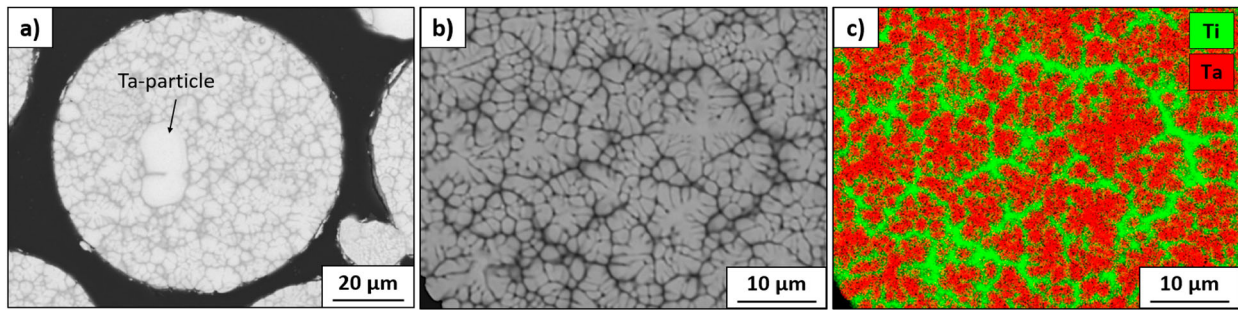


Figure 3. SEM results of pre-alloyed Ti-Ta powder particles: (a,b) Cross-section BSE images recorded at different magnifications and (c) EDS mapping illustrating the element distribution within the area shown in (b).

within the reconstructed 3D-volume investigated. The volume displayed ($4.4 \times 1.7 \times 1.4 \text{ mm}^3$) contains a total number of 76 detected pores, which are homogeneously distributed throughout the microstructure. From these data a relative density of 99.92% has been calculated for the PBF-EB/M processed Ti-Ta. While a maximum pore size of $140 \mu\text{m}$ can be detected, an average pore diameter (assuming a spherical shape) of $73 \mu\text{m}$ is found. The average pore sphericity, in turn, is determined to be 0.62 (the value 1 is representative for an ideally spherical shape). The coincidence of a spherical shape and small pore diameters points at gas porosity induced by hollow powder particles. The presence of such hollow particles is a well-known, however, a hardly avoidable phenomenon for additively manufactured metal structures fabricated based on gas-atomised powder feedstock material [49–51]. On the contrary, pores with larger diameters (and not being highly spherical in shape) can be attributed to local process instabilities like keyholing and lack of fusion, respectively

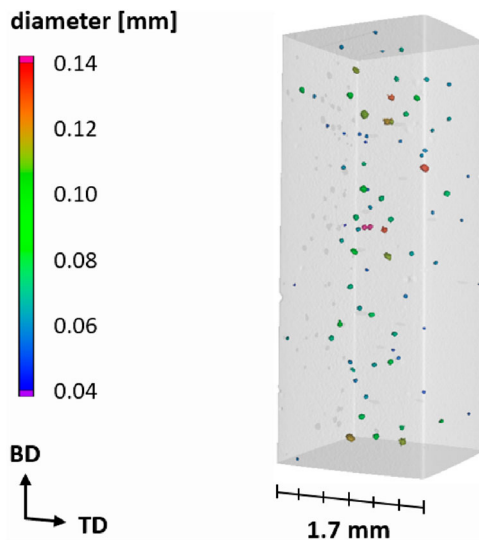


Figure 4. Computed tomography results of PBF-EB/M processed Ti-Ta in the as-built condition.

[49,51]. According to the average pore diameter and the sphericity value found, keyholing is supposed to be the dominant mechanism in the present work. Lack of fusion porosity [49], in turn, has been avoided with the set of processing parameters applied.

For initial microstructure characterisation after PBF-EB/M processing, the phase composition and grain structure were assessed using XRD analysis and SEM including EBSD, respectively. Figure 5 shows XRD diffraction patterns obtained at room temperature from the additively manufactured material in as-built condition (Figure 5(a)) and after solution-annealing at 1100°C for 25 h (Figure 5(b)). For the PBF-EB/M processed Ti-Ta in the as-built condition, the set of diffraction peaks indicates the presence of a β -phase stabilised microstructure. The lattice parameter is determined to be $a_\beta = 0.3286 \text{ nm}$, which is in line with data reported in literature [52,53].

Due to the relative high processing temperatures and the inherent low cooling rates within the process chamber after fabricating the uppermost layer, microstructures formed in titanium alloys during PBF-EB/M are often characterised by phase constitutions that are close to the equilibrium state [45,54,55]. The α/β transition temperature of Ti-Ta alloys depends on their chemical composition, i.e. the Ti:Ta ratio. According to the phase diagram [56], Ti-30Ta is an $\alpha+\beta$ dual-phase alloy in equilibrium. However, no traces of the α -phase are seen in the XRD pattern of the as-built condition (Figure 5(a)). In the present study, the solidification microstructure, i.e. the constituent phases after PBF-EB/M processing, can be rationalised based on the TTT diagram recently published by Paulsen et al. [17]. At this point, it has to be emphasized that the TTT plot (a CCT diagram is not available for the Ti-30Ta alloy in literature), only is used for schematic visualisation and interpretation (not for quantitative analysis). Being aware about the limitations of this approach, i.e. TTT plots are actually used for phase analysis after isothermal aging, Figure 1 is used to guide the discussion and the

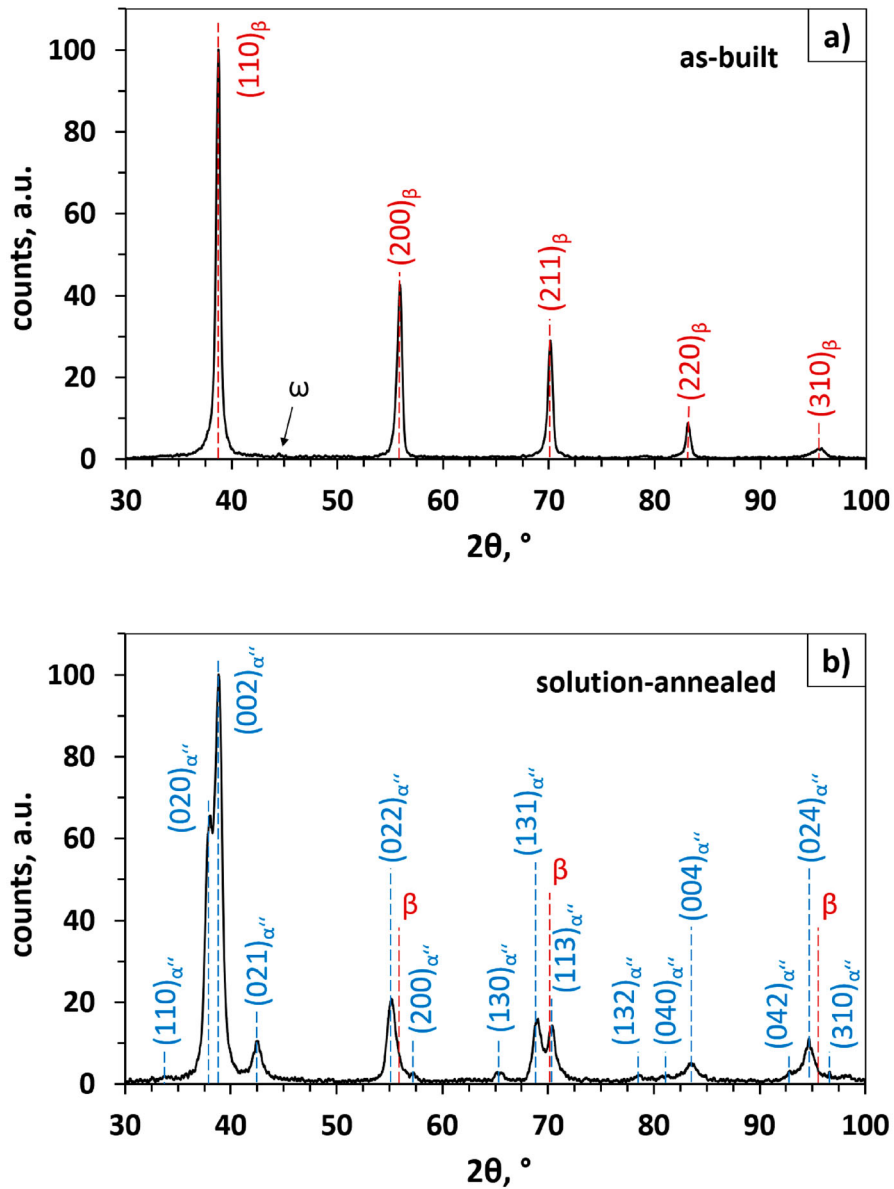


Figure 5. X-ray diffraction patterns of PBF-EB/M processed Ti-Ta in (a) as-built and (b) solution-annealed (25 h/1100°C) condition.

reader, respectively, on a qualitative basis. As can be seen from the temperature-time profile of the PBF-EB/M process and the simplified TTT plot (black curve in Figure 1), only the $\beta+\omega$ region is crossed upon processing and subsequent cooling. In the metastable state, i.e. after solution-annealing and rapid cooling to room temperature, ω -phase formation is suppressed and Ti-Ta alloys (7–36 at.% Ta) can show a diffusionless phase transformation from the high-temperature β -phase to the orthorhombic martensitic α'' -phase [13,56–58]. When subjected to critical temperature regimes (cf. TTT plot in Figure 1), however, the evolution of the isothermal ω -phase and the concomitant stabilisation of the high-temperature β -phase occur (cf. details discussed in Section 3.3) [13,17,21]. The dashed grey line

in Figure 1 borders the region where the orthorhombic α'' martensite can be found. Despite the β -stabilizing effect of the ω -phase, material states located on the left side of this line still show a martensitic transformation (to some extent). On the right side, in turn, α'' martensite is fully suppressed by the ω -phase formation [17], leading to fully β -stabilised conditions as found in the as-built condition (Figure 5(a)). Unfortunately, even relative high volume fractions of ω result in weak diffraction intensities in XRD pattern (cf. Figure 5(a) and Ref. [17]).

The grain morphology and crystallographic orientation of the β -phase are highlighted by the image quality (IQ) map (a), the inverse pole figure (IPF) orientation map (b), and the corresponding IPF recalculated from EBSD data (c) shown in Figure 6. The β -phase was

indexed with a bcc crystal structure (Im3m) and the lattice parameter obtained from the XRD diffraction pattern in Figure 5(a), i.e. $a_{\beta} = 0.3286$ nm. In general, microstructures formed during AM processes, such as PBF technologies and DED, are often dominated by strongly textured columnar grains oriented in BD, the main direction of heat flow [26,27]. For the materials most commonly fabricated by the PBF-EB/M technique, e.g. Ti-6Al-4 V and IN718, such highly anisotropic microstructures have been numerous reported in the past [59,60]. Solidification states in additively manufactured metallic materials are strongly affected by the relation between the temperature gradient (G) and the solidification rate (R) [61,62]. The high thermal gradient at the solid-liquid interface of the melt pool generally results in high G/R ratios, promoting epitaxial grain growth and eventually columnar grain structures with strong texture.

Unlike typical microstructures, the EBSD results in Figure 6 reveal mainly small equiaxed β -grains with almost random texture for the PBF-EB/M processed Ti-Ta. The average grain size is found to be $19.5 \mu\text{m}$. Minor variations of the grain size within the microstructure are visible. However, the underlying mechanism for these variations cannot be clarified at this point. The equiaxed microstructure is formed due to the high compositional solidification rate of the Ti-Ta alloy, which is driven by formation of Ta-rich solid phase upon solidification, leading to an increase in number of nucleation sites [63,64]. Several recent studies used PBF-LB/M and mixtures of elemental powders to successfully produce various Ti-Ta biomedical alloys [65–70]. Please note that only biomedical Ti-Ta alloys were focused in these studies that do not feature shape memory properties. In accordance with the results presented here, equiaxed β -phase microstructures were also observed. Constitutional supercooling seems to be the dominating

mechanism and act as the main driving force for the formation of an equiaxed microstructure in additively manufactured Ti-Ta alloys. Still, small regions of elongated grains with preferred $\langle 001 \rangle$ crystallographic orientation (cf. increased texture component in Figure 6(b)) are present throughout the microstructure (Figure 6(a)).

SEM analysis on the PBF-EB/M processed Ti-Ta at higher magnification reveals additional microstructural characteristics. Figure 7 shows BSE micrographs (a-c) and an EDS line scan (d) for the additively manufactured Ti-Ta in as-built condition. Three microstructural features are obvious from the micrographs: (1) overlapping melt pool structures of the individual scan tracks, (2) dendrite-type microsegregations, and (3) unmelted Ta-particles. The characteristic melt pool arrangement (Figure 7(a)) results from the bidirectional meander scanning strategy with 90° rotation between successive layers that was applied. Within the melt pools, in turn, dendritic features of different sizes and lengths can be seen in Figure 7(a-c). Both melt pool boundaries as well as dendrites have been reported for biomedical Ti-Ta alloys after processing of mixtures of elemental powders by PBF-LB/M technique [69,71]. During solidification of the Ti-Ta alloy, equilibrium state is difficult to be achieved by diffusion due to the highly different physical properties of the constituent elements. In consequence, the concentration of Ta is enriched in the solid phase fractions at the liquid-solid interface, while at the same time Ti is rejected into the liquid phase. Under such solidification conditions, dendrites are formed caused by compositional gradients of the solute elements ahead of the solidification front [69,71]. This leads to chemical fluctuations after PBF-EB/M as revealed by the EDS line scan in Figure 7(d). In addition to these microsegregations, the microstructure of the PBF-EB/M processed Ti-Ta comprised of randomly dispersed unmelted Ta-particles (Figure 7(a-c), exemplarily highlighted by the white

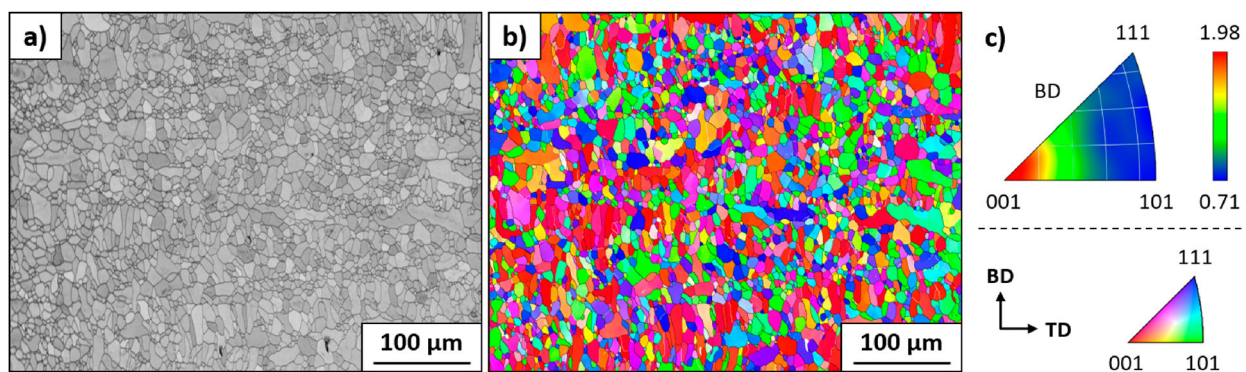


Figure 6. SEM EBSD results of PBF-EB/M processed Ti-Ta in the as-built condition: (a) Image quality (IQ) map, (b) inverse pole figure (IPF) orientation map, and (c) corresponding IPF. (b) and (c) highlight the crystallographic orientation of the parent β -phase with respect to BD. The reference coordinate system and the colour-coded standard triangle are shown in the lower right.

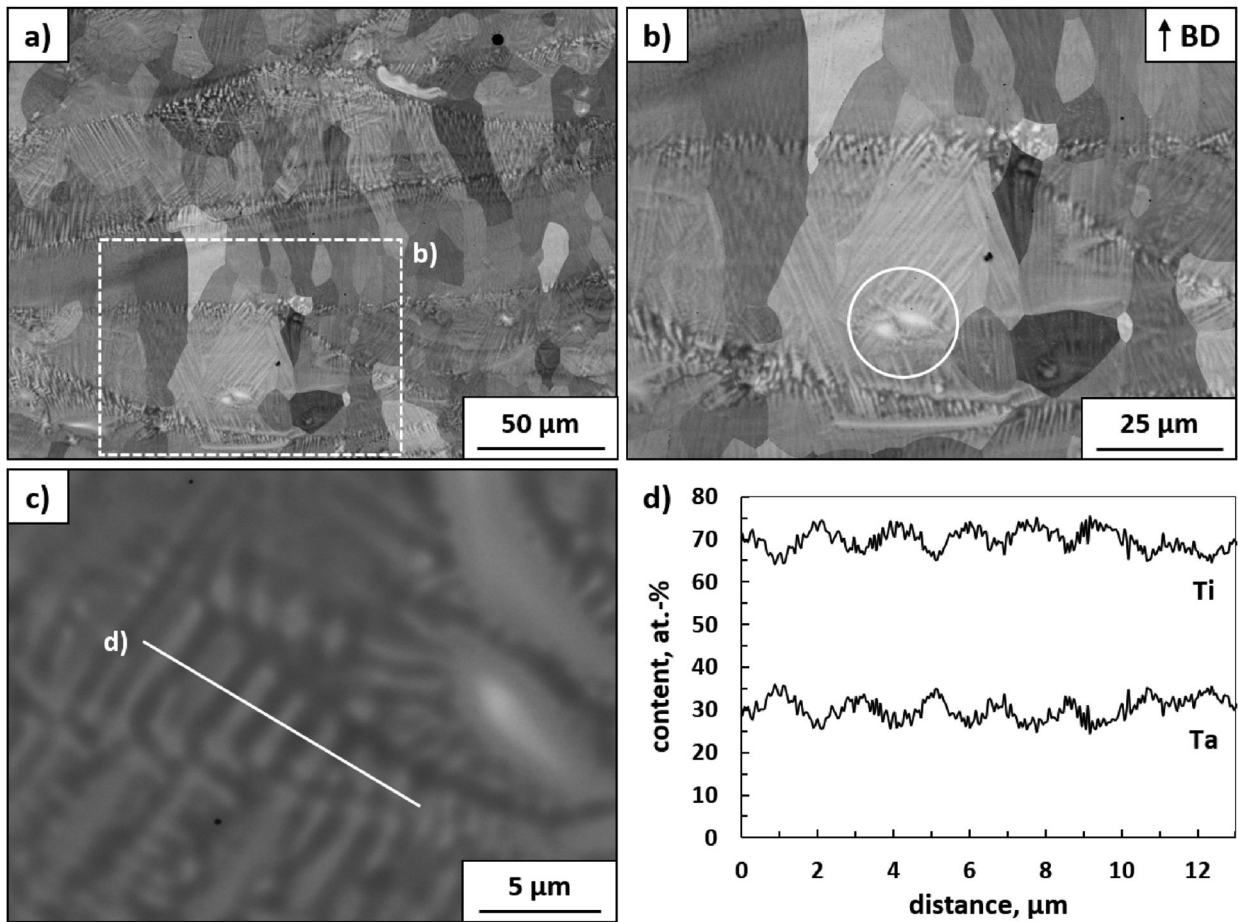


Figure 7. SEM results of PBF-EB/M processed Ti-Ta in as-built condition: (a-c) BSE images at different magnifications and (d) EDS line scan. The white circle in (b) exemplarily highlights unmelted Ta-particles found after processing. The position of the EDS line scan is marked by the white line in (c). BD is from bottom to top.

circle in (b). Elemental refractory particles have been recently shown to act as potent heterogeneous nucleation sites, promoting the columnar to equiaxed transition (CET) in titanium alloys [72]. Thus, it is expected that in addition to nucleation from constitutional supercooling, the unmelted Ta-particles additionally contribute to nucleation and development of the equiaxed microstructure in the as-built condition.

The remaining Ta-particles after PBF-EB/M stem from the initial powder feedstock material (Figure 3). The energy density applied during processing was sufficiently high to melt the pre-alloyed powder matrix, but too low to melt the Ta-particles within the powder material entirely. Unmelted refractory particles are frequently observed in additive manufacturing of elemental powder blends, especially when the energy input was too low [68–71,73,74]. So far, such *in situ* alloying approaches were the state-of-the-art for processing of refractory titanium alloys, such as Ti-Nb and Ti-Ta (please note that only biomedical Ti-Ta alloys were considered in these studies that do not feature shape

memory properties) [65–67,69,73,74], since pre-alloyed powder feedstock material was not available for a long time. However, due to the challenging alloy formation caused by the substantial differences in the melting points and densities of the alloying elements [10,75], these *in situ* alloying approaches suffered from material inhomogeneities after fabrication, i.e. the presence of unmolten Nb- and Ta-particles. While an increase of the energy input to fully melt the inhomogeneous powders caused substantial keyholing [69,73], some success was reported for remelting scanning strategies, i.e. repeated melting of the uppermost layer during additive manufacturing [65–67]. However, this approach decreases the productivity of the AM process and limits its applicability in manufacturing structures consisting of fine features. In contrast, pre-alloyed feedstock material can lead to excellent chemical homogeneity of Ti-based refractory alloys, as recently shown for Ti-Nb(-Ta) [46,47] and Ti-Ta-Al [45]. At this point, it should be emphasised that the fabrication of high quality powder feedstock material of Ti-based refractory alloys is highly

challenging, especially when the contents of the refractory constituents are high, as in the current study. Work on the powder processing route used (cf. Section 2.1) is already in progress to avoid (partly) unmelted Ta-particles after gas atomisation and, thus, to further improve the powder quality and resulting microstructure of the additively manufactured components.

3.2.2. Solution-annealing

In the field of shape memory technology, (post-process) thermo-mechanical treatments are effective approaches to establish microstructures that do not suffer from issues typically associated with solidification (uncontrolled precipitation, segregation of alloying elements, columnar grain formation, and/or solidification textures) [4,10,30]. In the present study, the metastable β microstructure of the as-built condition (cf. Figure 5(a)) is not adequate to demonstrate a martensitic transformation at elevated temperatures. In other words, the martensitic α'' -phase (orthorhombic) must be present at room temperature, which can transform into the austenitic β -phase

upon heating, leading to high-temperature shape memory properties. Furthermore, as the phase transformation temperatures of Ti-Ta HT-SMAs are very sensitive to the Ta content [12,13], microstructures with chemical heterogeneities, such as the dendrites (Figure 7), were reported to affect the functional properties [10]. Hence, a homogenisation and solution-annealing treatment at 1100°C for 25 h followed by water quenching was conducted after PBF-EB/M processing.

Figure 8 depicts BSE images recorded at different magnifications (a-c) and an EDS line scan (d) for the PBF-EB/M processed Ti-Ta in heat-treated condition. As can be deduced from the XRD pattern and the SEM results in Figures 4 and 7, respectively, the microstructure of the additively manufactured Ti-Ta has significantly changed upon post-process heat treatment. On the one hand, an equiaxed coarse-grained microstructure is observed for the heat-treated material state (Figure 8(a)). Using the line intercept method, the average grain size is determined to be about 70.4 μm , which is larger by a factor of 3.6 than that found in the

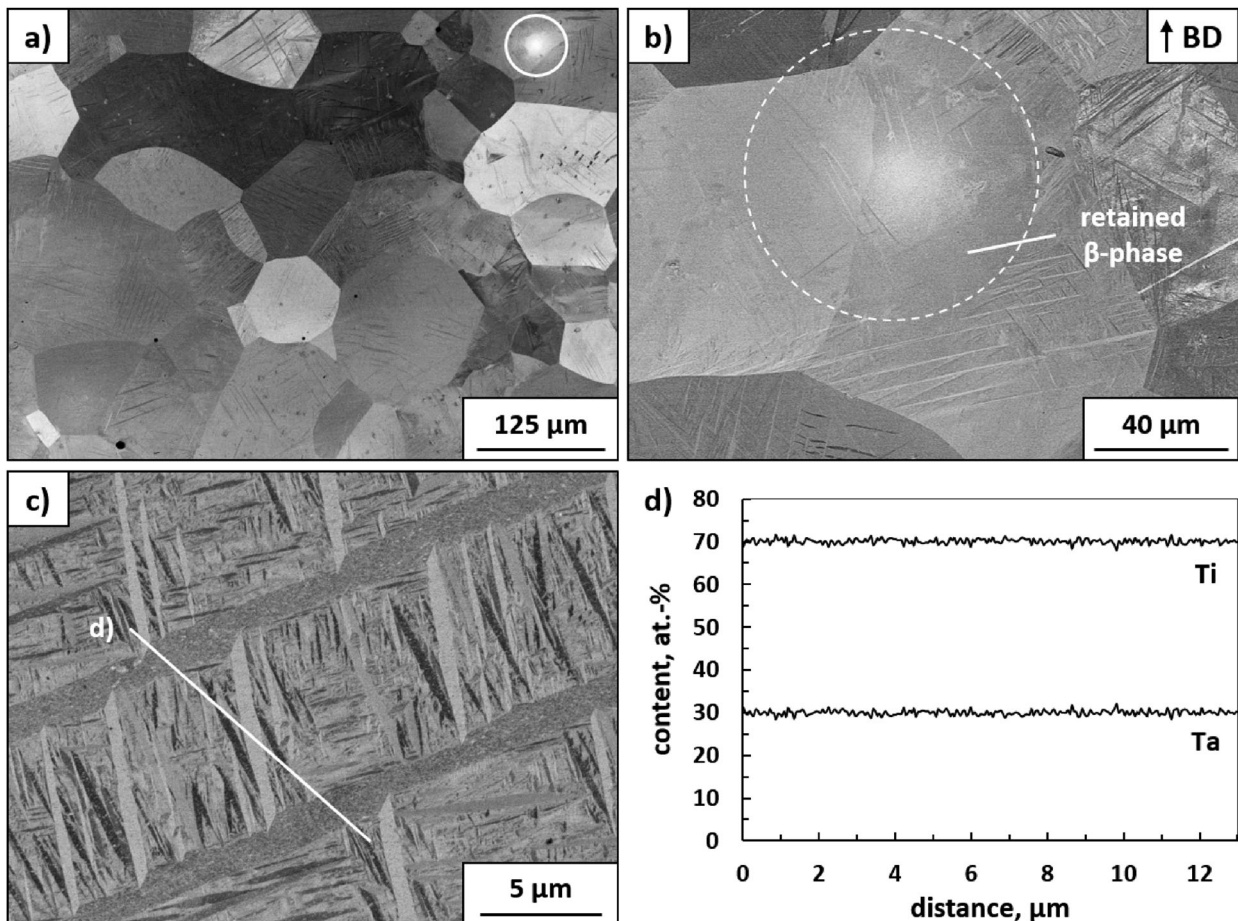


Figure 8. SEM results of PBF-EB/M processed Ti-Ta in solution-annealed condition: (a-c) BSE images at different magnifications and (d) EDS line scan. The white circles in (a) and (b) highlight remaining, not fully dissolved Ta-particles and diffusion areas with localised retained β -phase volume fractions after the thermal treatment, respectively. The position of the EDS line scan is marked by the white line in (c). BD is from bottom to top.

as-built condition (Figure 6). In titanium and its alloys, annealing treatments conducted in the single β -phase regime, i.e. above the β -transus temperature, are known to result in rapid coarsening of the β -grains [76]. On the other hand, the phase constitution changed from β to a predominantly martensitic microstructure after annealing and subsequent quenching (Figure 5(a,b)).

As already mentioned above, solution-annealed Ti-Ta alloys (7–36 at.% Ta) are free of ω -phase and undergo a martensitic transformation of type β (bcc) \rightarrow a'' (orthorhombic) upon quenching to room temperature [13,56–58]. In line with these observations, the XRD pattern in Figure 5(b) reveals a mainly martensitic microstructure consisting of the a'' -phase for the PBF-EB/M processed Ti-30Ta in heat-treated and quenched condition. The lattice parameters are $a_{a''} = 0.3083$ nm, $b_{a''} = 0.4948$ nm, and $c_{a''} = 0.4587$ nm. In addition to the non-equilibrium a'' -phase, however, tiny visible shoulders on specific diffraction peaks (cf. 2θ angles at around 56° , 70° , and 96° in Figure 5(b)) clearly hint at the presence of a secondary phase. The SEM/BSE results in Figure 8(a,b) indicate that a small amount of Ta-particles was present in the additively manufactured Ti-Ta material even after the homogenisation treatment. Instead of a complete dissolution, characteristic diffusion areas formed around the remaining Ta-particles, which are enriched in Ta (as revealed by EDS analysis, not shown for brevity). For Ti-Ta alloys, fully stabilised β -phase microstructures at room temperature were reported for Ta concentrations above 40 at.% [13]. Consequently, the volume fractions of the retained β -phase (cf. shoulders found on specific diffraction peaks in Figure 5(b)) can be attributed to the increased concentration of Ta within the diffusion areas surrounding the unmelted Ta-particles and its β -stabilizing effect. The SEM/BSE micrograph in Figure 8(b) gives clear evidence for the significantly lower density of martensite plates (a'' -phase) in these areas or, vice versa, the stabilisation of the high-temperature β -phase.

Even though the unmelted Ta-particles were not fully dissolved by the homogenisation treatment, the overall chemical homogeneity of the processed structures has been significantly improved upon the post-process thermal treatment. As can be seen from the EDS line scan in Figure 8(d), the chemical fluctuations that are seen in the microstructure of the as-built condition (cf. EDS line scan in Figure 7(d)) completely vanished after the heat treatment at 1100°C for 25 h. Zhang et al. [10] already reported dissolution of dendrites and, thus, significantly improved chemical homogeneity in conventionally processed Ti-Ta HT-SMAs upon solution-

annealing treatments at 1100°C . In summary, the microstructural analysis in the present work (Figures 4(b) and 6) reveals a predominantly martensitic microstructure with homogenous element distribution for the PBF-EB/M processed Ti-Ta in post-process heat-treated condition. The BSE contrast that is still visible in Figure 8(c) only results from the orientation contrast caused by the different martensite plates. However, the specific crystallographic orientation of the individual martensite plates cannot be assessed at this point. An EBSD measurement obtained for the martensitic structures is shown in the supplementary material, clearly revealing issues with indexing.

Such kind of martensitic microstructure presented after homogenisation treatment offers high potential for superior functional properties at elevated temperatures as will be outlined in the following. Beforehand, the authors finally note that achieving shape memory behaviour in additively manufactured (HT-)SMA structures without the need for any kind of post-process heat treatment is strongly anticipated. Such post-processing reduces the productivity of an AM technique and counteracts a fast and inexpensive fabrication of functional components for many envisioned applications. In general, a strong interrelationship between processing parameters applied, resulting microstructure and functional properties of additively manufactured (SMA) structures is known from the literature [77–80]. For PBF-LB/M processed Ni-Ti SMAs, for instance, Moghadam et al. [80] introduced a methodology to obtain a reversible martensitic phase transformation in as-built structures by an adequate choice of the processing parameters. The success of such effective approach to replace the post-process annealing with an *in situ* processing parameter setting in the Ti-Ta system, however, is seen as doubtful. As can be deduced from TTT-plot in Figure 1 and the temperature-time profile during PBF-EB/M processing, the precipitation kinetics of secondary phases, especially the ω -phase, are decisive for the resulting microstructure. Due to an improved microstructural stability, in future studies, ternary Al – and Sc-modified Ti-Ta compositions are seen to be very promising to obtain a martensitic microstructure after processing and, thus, functional properties in PBF-EB/M processed as-built conditions [21].

3.3. Martensitic phase transformation behaviour

In order to investigate the characteristic transformation temperatures and to assess the martensitic transformation behaviour upon thermal cycling, DSC measurements were conducted following the heat treatment at 1100°C for 25 h. Figure 9 shows two consecutive DSC

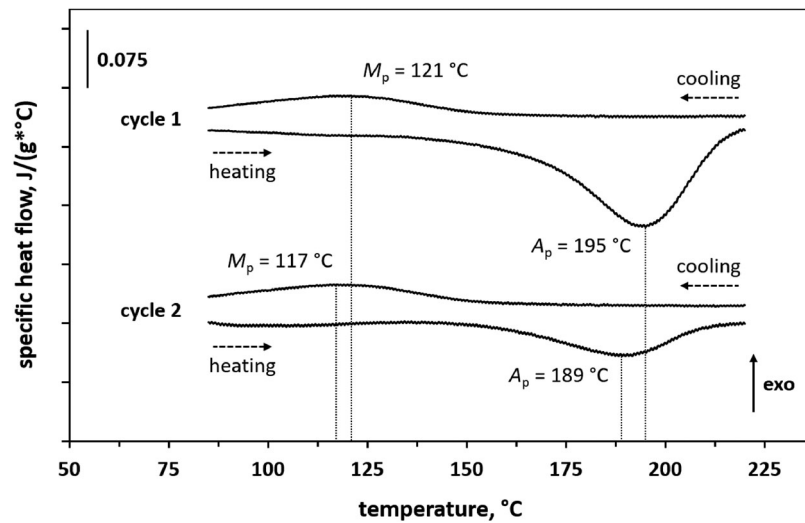


Figure 9. DSC curves of PBF-EB/M processed Ti-Ta in solution-annealed condition. The characteristic peak temperatures for the transformation into austenite (A_p) and martensite (M_p) upon heating and cooling are marked, respectively.

cycles for PBF-EB/M processed Ti-Ta in heat-treated condition, where strong transformation events can be observed. While the exothermic peaks on cooling are associated with the formation of martensite ($\beta \rightarrow \alpha'$), the endothermic reactions upon heating indicate the reverse transformation ($\alpha' \rightarrow \beta$). The additively manufactured Ti-Ta clearly demonstrates a reversible martensitic phase transformation at temperatures well above 100°C. Peak transformation temperatures of 195°C (A_p) and 121°C (M_p) are found for the first heating and subsequent cooling, respectively.

However, it is also obvious from the DSC data that the phase transformation behaviour is not stable and changes during thermal cycling. Two trends can be identified: (1) the transformation temperatures shift to lower values (cf. evolution A_p and M_p peak temperatures in Figure 9), and (2) the latent heat decreases, which can be derived from the area below the transformation peaks. The decrease in latent heat from the first to the second DSC cycle points at a smaller volume fraction of the material that undergoes forward and reverse martensitic transformations during thermal cycling. This indicates that the reversibility of the martensitic phase transformation is significantly affected by the evolution of microstructural features during heating and cooling. Both effects, i.e. the shift of the transformation temperatures and a reduction in the transforming volume, were reported in a series of studies for conventionally processed Ti-Ta HT-SMAs after thermal aging as well as under thermal and thermo-mechanical cycling conditions [11,13,15–17,20,21,25]. The formation of ω -phase was ascribed as the primary underlying microstructural mechanism for the functional degradation (cf. discussion below).

In order to prove the presence of the ω -phase upon thermal cycling in the present study, the microstructure has been investigated by TEM. Figure 10 shows the *post-mortem* TEM results for the PBF-EB/M processed Ti-Ta. The selected area electron diffraction (SAED) pattern taken from the $[0\bar{1}1]_\beta$ zone axis (Figure 10(a)) reveals weak and diffuse streaking between main β -phase reflections. For more clarity, a 3D surface plot is presented in Figure 10(b), which illustrates the minor intensity peaks at $1/3$ and $2/3 \langle 112 \rangle_\beta$. It is well-known that these peaks correspond to the hexagonal ω -phase (marked by red arrows). The highly diffuse character of these extra spots indicates an initial stage of ω -phase formation (often referred to as incommensurate ω -phase [81]), which is fully in line with the DSC results (Figure 9) as detailed in the following.

In metastable β -type Ti-based alloys, such as Ti-Nb, Ti-Mo, and Ti-Ta, the (isothermal) ω -phase can form when these alloys are subjected to heat treatments above 100°C [82]. Due to its utmost importance for the stability of the functional properties, the kinetics of the ω -phase formation were recently assessed for the Ti-Ta system based on a TTT diagram (cf. Figure 1) [17]. In the present study, the ω -phase is considered to precipitate during thermal cycling. Its formation is accompanied by the enrichment of the β -stabilizing element Ta within the β -phase matrix, as ω was found to be rich in Ti [17]. On the one hand, this causes the observed shift of the martensitic transformation temperatures, since the transformation behaviour of Ti-Ta HT-SMAs is strongly dependent on the concentration of Ta [12,13]. On the other hand, the parent β -phase is stabilised simultaneously, resulting in a suppression of the martensitic transformation [10,17,21], as indicated by the decrease

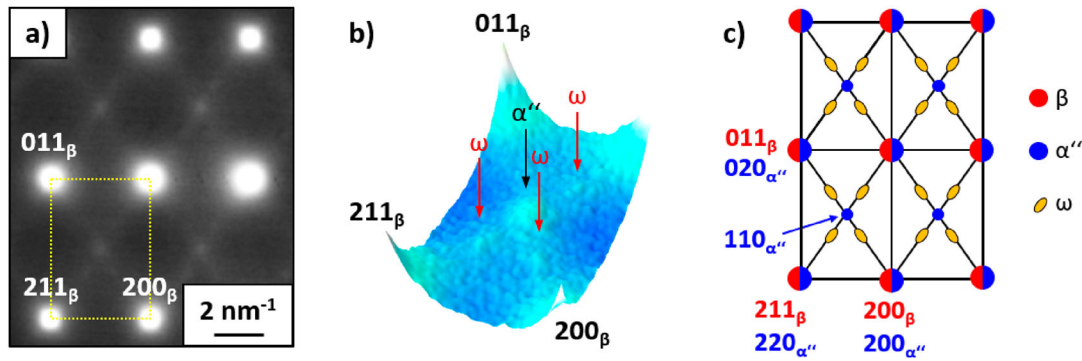


Figure 10. TEM results of PBF-EB/M processed Ti-Ta in solution-annealed condition after being subjected to the DSC tests shown in Figure 9: (a) SAED pattern taken from $[0\bar{1}1]_{\beta}$ zone axis, (b) 3D surface plot of the rectangular region marked in (a), and (c) indexed key diagram of the diffraction pattern in (a), revealing an overlapping of selected β and α'' reflections. See main text for details.

in latent heat (cf. Figure 9). It was reported that ω -phase formation can result even in a complete loss of the functional properties [11,15–17,20]. Following the two DSC cycles conducted, however, the PBF-EB/M processed Ti-Ta is not fully degraded. Upon the second cooling (lower cycle in Figure 9), the phase transformation from the high-temperature β -phase into the low-temperature martensitic phase is not fully suppressed, showing a visible transformation peak. In accordance with this result, the *post-mortem* TEM analysis reveals additional peaks at $1/2 \langle 112 \rangle_{\beta}$ determined to correspond to the orthorhombic martensite α'' . Thus, a multi-phase microstructure consisting of a $\beta + \alpha''$ dual-phase matrix and isothermally formed ω -phase (Figure 10) is found after DSC testing. The latter phase, in turn, is supposed to be in its initial precipitation stages (cf. low intensity diffraction spots in Figure 10), still allowing functional properties in the Ti-Ta material.

It is well documented that the microstructural and functional stability of Ti-Ta HT-SMAs under thermal and thermo-mechanical cycling strongly depend on the testing conditions, such as the applied heating/cooling rates and maximum test temperatures [10,15,16]. In the present study, the transformation temperatures upon first heating (upper cycle in Figure 9), i.e. austenite start ($A_s = 165^{\circ}\text{C}$), peak ($A_p = 195^{\circ}\text{C}$), and finish temperature ($A_f = 214^{\circ}\text{C}$), are in good agreement with those of conventionally processed Ti-30Ta HT-SMAs [10,17]. In contrast, the transformation temperatures during subsequent cooling clearly differ from data being available in literature [10,17]. Upon subsequent cooling, the DSC chart reveals a flattened transformation peak and, thus, only the martensite peak temperature (M_p) has been determined. A peak temperature of $M_p = 121^{\circ}\text{C}$ in the first cycle is significantly lower compared to values reported in previous studies reporting on conventionally processed counterparts [10,17,21]. Both the flattened transformation peak and

the decrease in transformation temperatures indicate that the transformation behaviour of the PBF-EB/M processed Ti-Ta is affected by ω -phase formation in the initial DSC cycle. In general, its evolution is known to be relatively fast, as ω can be immediately seen after aging for a short time (cf. Figure 1) [17]. However, despite the same heating/cooling rate of 20 K/min and even a lower maximum test temperature applied, formation of isothermal ω -phase appears to be even more rapid in the additively manufactured material than in conventionally processed Ti-Ta alloys [10,17,21]. Future efforts are required to verify whether the precipitation kinetics are different. Likewise, the influence of the unmelted and not fully dissolved Ta-particles cannot be fully clarified at this point and requires ongoing work. Beside the well-known effect of Ta on the transformation temperatures [12,13], remaining particles may also act as strong obstacles during martensitic transformation, eventually affecting the shape (width) of the DSC peaks or even the reversibility of the phase transformation.

4. Conclusions

In the present study, a Ti-30Ta (at.%) high-temperature shape memory alloy (HT-SMA) was successfully processed by electron beam powder bed fusion (PBF-EB/M) using pre-alloyed powder. The microstructure of the powder feedstock material and additively manufactured Ti-Ta structures in both as-built and post-process heat-treated condition have been investigated in depth. Furthermore, the martensitic transformation behaviour and its evolution upon thermal cycling have been assessed. The main findings can be summarised as follows:

- Pre-alloyed feedstock material with highly spherical powder particles has been obtained by electrode induction melting inert gas atomisation (EIGA). Except for a few remaining Ta-particles being not

fully dissolved during EIGA processing, the powder particles feature only slight chemical inhomogeneities, i.e. dendrite-type microsegregations with Ta-rich dendrites embedded in a Ti-rich matrix.

- Additively manufactured bulk structures with a density of 99.92% have been obtained by PBF-EB/M technique. A near isotropic, β -phase (bcc) stabilised microstructure with mainly equiaxed grains and almost random texture is observed in the as-built condition.
- After a post-process thermal treatment at 1100°C for 25 h followed by water quenching, a predominantly martensitic microstructure, consisting of the non-equilibrium orthorhombic α'' -phase, is present. Minor volume fractions of retained β -phase are also found and can be attributed to their stabilisation within the diffusion areas surrounding the partially melted Ta-particles, where the concentration of the β -stabilizing element Ta is significantly increased.
- Post-process heat-treated Ti-Ta shows a reversible martensitic transformation well above 100°C. In turn, the transformation temperatures and the reversibility of the phase transformation upon thermal cycling are strongly affected by the formation of the ω -phase.

Acknowledgements

The authors acknowledge the facilities, and the scientific and technical assistance of the RMIT University's Microscopy & Microanalysis Facility, a linked laboratory of the Microscopy Australia, enabled by NCRIS. Nadia Zakhartchouk, a member of the Analytical Chemistry Technical Team at RMIT University Melbourne, is thanked for her assistance with the experiments.

Disclosure statement

No potential conflict of interest was reported by the author(s).

Funding

This work was supported by Alexander von Humboldt-Stiftung.

Data availability statement

The data that support the findings of this study are available from the corresponding author, CL, upon reasonable request.

ORCID

C. Lauhoff  <http://orcid.org/0000-0003-1708-6026>
 A. Medvedev  <http://orcid.org/0000-0003-0336-569X>
 P. Krooß  <http://orcid.org/0000-0001-8310-9631>
 M. Weinmann  <http://orcid.org/0000-0002-9029-7535>
 A. Molotnikov  <http://orcid.org/0000-0002-2338-0101>
 T. Niendorf  <http://orcid.org/0000-0003-2622-5817>

References

- [1] Lagoudas DC. Shape memory alloys: modeling and engineering applications, 2008.
- [2] Otsuka K, editor. *Shape memory materials*. 1st ed. Cambridge: Cambridge University Press; 1999.
- [3] Duerig TW, Melton KN, Stöckel D, et al. *Engineering aspects of shape memory alloys*. Elsevier; 1990.
- [4] Elahinia MH, Hashemi M, Tabesh M, et al. Manufacturing and processing of NiTi implants: a review. *Prog Mater Sci*. 2012;57:911–946. doi:10.1016/j.pmatsci.2011.11.001
- [5] Otsuka K, Ren X. Physical metallurgy of Ti–Ni-based shape memory alloys. *Prog Mater Sci* 2005;50:511–678. doi:10.1016/j.pmatsci.2004.10.001
- [6] Ma J, Karaman I, Noebe RD. High temperature shape memory alloys. *Int Mater Rev*. 2010;55:257–315. doi:10.1179/095066010X12646898728363
- [7] Sehitoglu H, Patriarca L, Wu Y. Shape memory strains and temperatures in the extreme. *Curr Opin Solid State Mater Sci*. 2017;21:113–120. doi:10.1016/j.cossms.2016.06.005
- [8] Canadinc D, Trehern W, Ozcan H, et al. On the deformation response and cyclic stability of Ni50Ti35Hf15 high temperature shape memory alloy wires. *Scr Mater* 2017;135:92–96. doi:10.1016/j.scriptamat.2017.03.025
- [9] Paulsen A, Dumlu H, Piorunek D, et al. Laboratory-scale processing and performance assessment of Ti–Ta high-temperature shape memory spring actuators. *Shap Mem Superelasticity*. 2021;7:222–234. doi:10.1007/s40830-021-00334-1
- [10] Zhang J, Rynko R, Frenzel J, et al. Ingot metallurgy and microstructural characterization of Ti–Ta alloys. *Int J Mater Res*. 2014;105:156–167. doi:10.3139/146.111010
- [11] Niendorf T, Krooß P, Batyrsina E, et al. Functional and structural fatigue of titanium tantalum high temperature shape memory alloys (HT SMAs). *Mater Sci Eng, A*. 2015;620:359–366. doi:10.1016/j.msea.2014.10.038
- [12] Chakraborty T, Rogal J, Drautz R. Unraveling the composition dependence of the martensitic transformation temperature: a first-principles study of Ti–Ta alloys. *Phys Rev B*. 2016;94:224104. doi:10.1103/PhysRevB.94.224104
- [13] Buenconsejo PJS, Kim HY, Hosoda H, et al. Shape memory behavior of Ti–Ta and its potential as a high-temperature shape memory alloy. *Acta Mater*. 2009;57:1068–1077. doi:10.1016/j.actamat.2008.10.041
- [14] Ferrari A, Paulsen A, Frenzel J, et al. Unusual composition dependence of transformation temperatures in Ti–Ta–X shape memory alloys. *Phys Rev Materials*. 2018;2:073609. doi:10.1103/PhysRevMaterials.2.073609
- [15] Niendorf T, Krooß P, Batyrsina E, et al. On the functional degradation of binary titanium–tantalum high-temperature shape memory alloys — a new concept for fatigue life extension. *Funct Mater Lett*. 2014;07:1450042. doi:10.1142/S1793604714500428
- [16] Maier HJ, Karsten E, Paulsen A, et al. Microstructural evolution and functional fatigue of a Ti–25Ta high-temperature shape memory alloy. *J Mater Res*. 2017;32:4287–4295. doi:10.1557/jmr.2017.319
- [17] Paulsen A, Frenzel J, Langenkämper D, et al. A kinetic study on the evolution of martensitic transformation behavior and microstructures in Ti–Ta high-temperature shape-memory alloys during aging. *Shap Mem*

- Superelasticity. 2019;5:16–31. doi:10.1007/s40830-018-00200-7
- [18] Kim HY, Ikehara Y, Kim JI, et al. Martensitic transformation, shape memory effect and superelasticity of Ti–Nb binary alloys. *Acta Mater.* 2006;54:2419–2429. doi:10.1016/j.actamat.2006.01.019
- [19] Bönisch M, Calin M, Waitz T, et al. Thermal stability and phase transformations of martensitic Ti–Nb alloys. *Sci Technol Adv Mater* 2013;14:055004. doi:10.1088/1468-6996/14/5/055004
- [20] Niendorf T, Krooß P, Somsen C, et al. Cyclic degradation of titanium–tantalum high-temperature shape memory alloys — the role of dislocation activity and chemical decomposition. *Funct Mater Lett.* 2015;08:1550062. doi:10.1142/S1793604715500629
- [21] Ferrari A, Paulsen A, Langenkämper D, et al. Discovery of ω -free high-temperature Ti–Ta–X shape memory alloys from first-principles calculations. *Phys Rev Materials.* 2019;3:103605. doi:10.1103/PhysRevMaterials.3.103605
- [22] Buenconsejo PJS, Kim HY, Miyazaki S. Novel β -TiTaAl alloys with excellent cold workability and a stable high-temperature shape memory effect. *Scr Mater* 2011;64:1114–1117. doi:10.1016/j.scriptamat.2011.03.004
- [23] Kim HY, Fukushima T, Buenconsejo PJS, et al. Martensitic transformation and shape memory properties of Ti–Ta–Sn high temperature shape memory alloys. *Mater Sci Eng, A.* 2011;528:7238–7246. doi:10.1016/j.msea.2011.06.021
- [24] Zheng XH, Sui JH, Zhang X, et al. Thermal stability and high-temperature shape memory effect of Ti–Ta–Zr alloy. *Scr Mater* 2013;68:1008–1011. doi:10.1016/j.scriptamat.2013.03.008
- [25] Buenconsejo PJS, Kim HY, Miyazaki S. Effect of ternary alloying elements on the shape memory behavior of Ti–Ta alloys. *Acta Mater.* 2009;57:2509–2515. doi:10.1016/j.actamat.2009.02.007
- [26] DebRoy T, Wei HL, Zuback JS, et al. Additive manufacturing of metallic components – process, structure and properties. *Prog Mater Sci* 2018;92:112–224. doi:10.1016/j.pmatsci.2017.10.001
- [27] Hitzler L, Merkel M, Hall W, et al. A review of metal fabricated with laser- and powder-bed based additive manufacturing techniques: process, nomenclature, materials, achievable properties, and its utilization in the medical sector. *Adv Eng Mater* 2018;20:1700658. doi:10.1002/adem.201700658
- [28] Li N, Huang S, Zhang G, et al. Progress in additive manufacturing on new materials: a review. *J Mater Sci Technol.* 2019;35:242–269. doi:10.1016/j.jmst.2018.09.002
- [29] Gorsse S, Hutchinson C, Gouné M, et al. Additive manufacturing of metals: a brief review of the characteristic microstructures and properties of steels, Ti–6Al–4V and high-entropy alloys. *Sci Technol Adv Mater.* 2017;18:584–610. doi:10.1080/14686996.2017.1361305
- [30] Elahinia M, Shayesteh Moghaddam N, Taheri Andani M, et al. Fabrication of NiTi through additive manufacturing: a review. *Prog Mater Sci* 2016;83:630–663. doi:10.1016/j.pmatsci.2016.08.001
- [31] Alagha AN, Hussain S, Zaki W. Additive manufacturing of shape memory alloys: a review with emphasis on powder bed systems. *Mater Des* 2021;204:109654. doi:10.1016/j.matdes.2021.109654
- [32] Toker GP, Nematollahi M, Saghaian SE, et al. Shape memory behavior of NiTiHf alloys fabricated by selective laser melting. *Scr Mater* 2020;178:361–365. doi:10.1016/j.scriptamat.2019.11.056
- [33] Elahinia M, Shayesteh Moghaddam N, Amerinatanzi A, et al. Additive manufacturing of NiTiHf high temperature shape memory alloy. *Scr Mater* 2018;145:90–94. doi:10.1016/j.scriptamat.2017.10.016
- [34] Gustmann T, Schwab H, Kühn U, et al. Selective laser remelting of an additively manufactured Cu–Al–Ni–Mn shape-memory alloy. *Mater Des* 2018;153:129–138. doi:10.1016/j.matdes.2018.05.010
- [35] Gustmann T, Neves A, Kühn U, et al. Influence of processing parameters on the fabrication of a Cu–Al–Ni–Mn shape-memory alloy by selective laser melting. *Addit Manuf.* 2016;11:23–31. doi:10.1016/j.addma.2016.04.003
- [36] Laitinen V, Sozinov A, Saren A, et al. Laser powder bed fusion of Ni–Mn–Ga magnetic shape memory alloy. *Addit Manuf.* 2019;30:100891. doi:10.1016/j.addma.2019.100891
- [37] Scheibel F, Lauhoff C, Krooß P, et al. Additive manufacturing of Ni–Mn–Sn shape memory Heusler alloy – microstructure and magnetic properties from powder to printed parts. *Materialia.* 2023;29:101783. doi:10.1016/j.mtla.2023.101783
- [38] Lauhoff C, Fischer A, Sobrero C, et al. Additive manufacturing of Co–Ni–Ga high-temperature shape memory alloy: processability and phase transformation behavior. *Metall Mater Trans A.* 2020;51:1056–1061. doi:10.1007/s11661-019-05608-z
- [39] Lauhoff C, Sommer N, Vollmer M, et al. Excellent superelasticity in a Co–Ni–Ga high-temperature shape memory alloy processed by directed energy deposition. *Mater Res Lett.* 2020;8:314–320. doi:10.1080/21663831.2020.1756495
- [40] Ormanova M, Dechev D, Ivanov N, et al. Synthesis and characterization of Ti–Ta-shape memory surface alloys formed by the electron-beam additive technique. *Coatings.* 2022;12:678. doi:10.3390/coatings12050678
- [41] Xiao B, Jia W, Tang H, et al. Microstructure and mechanical properties of WMoTaNbTi refractory high-entropy alloys fabricated by selective electron beam melting. *J Mater Sci Technol.* 2022;108:54–63. doi:10.1016/j.jmst.2021.07.041
- [42] Xiao B, Jia W, Tang H, et al. Microstructure and mechanical properties of a newly developed WTaRe refractory alloy by selective electron beam melting. *Addit Manuf.* 2022;54:102738. doi:10.1016/j.addma.2022.102738
- [43] Ledford C, Fernandez-Zelaia P, Graening T, et al. Microstructure and high temperature properties of tungsten processed via electron beam melting additive manufacturing. *Int J Refract Met Hard Mater.* 2023;113:106148. doi:10.1016/j.ijrmhm.2023.106148
- [44] Golod VM, Sufiarov VS. The evolution of structural and chemical heterogeneity during rapid solidification at gas atomization. *IOP Conf Ser: Mater Sci Eng* 2017;192:012009. doi:10.1088/1757-899X/192/1/012009
- [45] Lauhoff C, Arold T, Bolender A, et al. Microstructure of an additively manufactured Ti–Ta–Al alloy using novel pre-alloyed powder feedstock material. *Addit Manuf Lett.* 2023;6:100144. doi:10.1016/j.addlet.2023.100144

- [46] Schulze C, Weinmann M, Schweigel C, et al. Mechanical properties of a newly additive manufactured implant material based on Ti-42Nb. *Materials* (Basel). 2018;11:124. doi:10.3390/ma11010124
- [47] Johannsen J, Lauhoff C, Stenzel M, et al. Laser beam powder bed fusion of novel biomedical titanium/niobium/tantalum alloys: powder synthesis, microstructure evolution and mechanical properties. *Mater Des* 2023;112265. doi:10.1016/j.matdes.2023.112265
- [48] Couret A, Allen M, Rackel MW, et al. Chemical heterogeneities in tungsten containing TiAl alloys processed by powder metallurgy. *Materialia*. 2021;18:101147. doi:10.1016/j.mtla.2021.101147
- [49] Brennan MC, Keist JS, Palmer TA. Defects in metal additive manufacturing processes. *J Mater Eng Perform*. 2021;30:4808–4818. doi:10.1007/s11665-021-05919-6
- [50] Chen G, Zhou Q, Zhao SY, et al. A pore morphological study of gas-atomized Ti-6Al-4V powders by scanning electron microscopy and synchrotron X-ray computed tomography. *Powder Technol*. 2018;330:425–430. doi:10.1016/j.powtec.2018.02.053
- [51] Sola A, Nouri A. Microstructural porosity in additive manufacturing: the formation and detection of pores in metal parts fabricated by powder bed fusion. *J Adv Manuf Process*. 2019;1:10021. doi:10.1002/amp2.10021
- [52] Ferrari A, Kadletz PM, Chakraborty T, et al. Reconciling experimental and theoretical data in the structural analysis of Ti-Ta shape-memory alloys. *Shap Mem Superelasticity*. 2019;5:6–15. doi:10.1007/s40830-018-00201-6
- [53] Kadletz PM, Motemani Y, Iannotta J, et al. Crystallographic structure analysis of a Ti-Ta thin film materials library fabricated by combinatorial magnetron sputtering. *ACS Comb Sci* 2018;20:137–150. doi:10.1021/acscombsci.7b00135
- [54] Liu S, Shin YC. Additive manufacturing of Ti6Al4V alloy: a review. *Mater Des* 2019;164:107552. doi:10.1016/j.matdes.2018.107552
- [55] Hao Y-L, Li S-J, Yang R. Biomedical titanium alloys and their additive manufacturing. *Rare Met*. 2016;35:661–671. doi:10.1007/s12598-016-0793-5
- [56] Murray JL. The Ta–Ti (tantalum-titanium) system. *Bull Alloy Phase Diagrams*. 1981;2:62–66. doi:10.1007/BF02873705
- [57] Ikeda M, Komatsu S-y, Nakamura Y. The effect of Ta content on phase constitution and aging behavior of Ti-Ta binary alloys. *Mater Trans* 2002;43:2984–2990. doi:10.2320/matertrans.43.2984
- [58] Bywater KA, Christian JW. Martensitic transformations in titanium-tantalum alloys. *Philos Mag* 1972;25:1249–1273. doi:10.1080/14786437208223852
- [59] Fu Z, Körner C. Actual state-of-the-art of electron beam powder bed fusion. *Eur J Mater*. 2022;2:54–116. doi:10.1080/26889277.2022.2040342
- [60] Körner C. Additive manufacturing of metallic components by selective electron beam melting — a review. *Int Mater Rev*. 2016;61:361–377. doi:10.1080/09506608.2016.1176289
- [61] Collins PC, Brice DA, Samimi P, et al. Microstructural control of additively manufactured metallic materials. *Annu Rev Mater Res* 2016;46:63–91. doi:10.1146/annurev-matsci-070115-031816
- [62] Gäumann M, Henry S, Cléton F, et al. Epitaxial laser metal forming: analysis of microstructure formation. *Mater Sci Eng, A*. 1999;271:232–241. doi:10.1016/S0921-5093(99)00202-6
- [63] Kumar Mohanty U, Sarangi H. Solidification of Metals and Alloys. In: Abdallah Z, Aldoumani N, editors. *Casting processes and modelling of metallic materials*. London: IntechOpen; 2021.
- [64] Kurz W, Fisher DJ. *Fundamentals of solidification*. Zurich: Trans Tech Publications, Limited; 1998.
- [65] Brodie EG, Medvedev AE, Frith JE, et al. Remelt processing and microstructure of selective laser melted Ti25Ta. *J Alloys Compd*. 2020;820:153082. doi:10.1016/j.jallcom.2019.153082
- [66] Brodie EG, Richter J, Wegener T, et al. Influence of a remelt scan strategy on the microstructure and fatigue behaviour of additively manufactured biomedical Ti65Ta efficiently assessed using small scale specimens. *Int J Fatigue*. 2022;162:106944. doi:10.1016/j.ijfatigue.2022.106944
- [67] Brodie EG, Richter J, Wegener T, et al. Low-cycle fatigue performance of remelted laser powder bed fusion (L-PBF) biomedical Ti25Ta. *Mater Sci Eng, A*. 2020;798:140228. doi:10.1016/j.msea.2020.140228
- [68] Sing SL, Yeong WY, Wiria FE. Selective laser melting of titanium alloy with 50 wt% tantalum: microstructure and mechanical properties. *J Alloys Compd*. 2016;660:461–470. doi:10.1016/j.jallcom.2015.11.141
- [69] Huang S, Sing SL, de Looze G, et al. Laser powder bed fusion of titanium-tantalum alloys: compositions and designs for biomedical applications. *J Mech Behav Biomed Mater*. 2020;108:103775. doi:10.1016/j.jmbbm.2020.103775
- [70] Brodie EG, Wegener T, Richter J, et al. A mechanical comparison of alpha and beta phase biomedical TiTa lattice structures. *Mater Des* 2021;212:110220. doi:10.1016/j.matdes.2021.110220
- [71] Xing L-L, Zhao C-C, Chen H, et al. Microstructure of a Ti–50 wt% Ta alloy produced via laser powder bed fusion. *Acta Metall Sin* 2020;33:981–990. doi:10.1007/s40195-020-01052-w
- [72] Tedman-Jones SN, McDonald SD, Bermingham MJ, et al. A new approach to nuclei identification and grain refinement in titanium alloys. *J Alloys Compd*. 2019;794:268–284. doi:10.1016/j.jallcom.2019.04.224
- [73] Fischer M, Joguet D, Robin G, et al. In situ elaboration of a binary Ti-26Nb alloy by selective laser melting of elemental titanium and niobium mixed powders. *Mater Sci Eng, C*. 2016;62:852–859. doi:10.1016/j.msec.2016.02.033
- [74] Huang S, Narayan RL, Tan JHK, et al. Resolving the porosity-unmelted inclusion dilemma during in-situ alloying of Ti34Nb via laser powder bed fusion. *Acta Mater*. 2021;204:116522. doi:10.1016/j.actamat.2020.116522
- [75] Morita A, Fukui H, Tadano H, et al. Alloying titanium and tantalum by cold crucible levitation melting (CCLM) furnace. *Mater Sci Eng, A*. 2000;280:208–213. doi:10.1016/S0921-5093(99)00668-1
- [76] Polmear I, St John D, Nie J-F, et al. *Light alloys: metallurgy of the light metals*. 5th ed. [Place of publication not identified]: Elsevier Science and Technology Books, Inc; 2017.
- [77] Lu HZ, Ma HW, Cai WS, et al. Stable tensile recovery strain induced by a Ni4Ti3 nanoprecipitate in a Ni50.4Ti49.6 shape memory alloy fabricated via selective laser

- melting. *Acta Mater.* 2021;219:117261. doi:[10.1016/j.actamat.2021.117261](https://doi.org/10.1016/j.actamat.2021.117261)
- [78] Lu HZ, Ma HW, Luo X, et al. Microstructure, shape memory properties, and in vitro biocompatibility of porous NiTi scaffolds fabricated via selective laser melting. *J Mater Res Technol.* 2021;15:6797–6812. doi:[10.1016/j.jmrt.2021.11.112](https://doi.org/10.1016/j.jmrt.2021.11.112)
- [79] Luo X, Liu LH, Yang C, et al. Overcoming the strength–ductility trade-off by tailoring grain-boundary metastable Si-containing phase in β -type titanium alloy. *J Mater Sci Technol.* 2021;68:112–123. doi:[10.1016/j.jmst.2020.06.053](https://doi.org/10.1016/j.jmst.2020.06.053)
- [80] Shayesteh Moghaddam N, Saedi S, Amerinatanzi A, et al. Achieving superelasticity in additively manufactured NiTi in compression without post-process heat treatment. *Sci Rep.* 2019;9:41. doi:[10.1038/s41598-018-36641-4](https://doi.org/10.1038/s41598-018-36641-4)
- [81] Ballor J, Li T, Prima F, et al. A review of the metastable omega phase in beta titanium alloys: the phase transformation mechanisms and its effect on mechanical properties. *Int Mater Rev.* 2023;68:26–45. doi:[10.1080/09506608.2022.2036401](https://doi.org/10.1080/09506608.2022.2036401)
- [82] Hickman BS. The formation of omega phase in titanium and zirconium alloys: a review. *J Mater Sci.* 1969;4:554–563. doi:[10.1007/BF00550217](https://doi.org/10.1007/BF00550217)